Geometrical and Monte Carlo projectors in 3D PET reconstruction

Pablo Aguiar[a)]
Fundación IDICHUS/IDIS, Complexo Hospitalario Universitario de Santiago de Compostela, Departamento de Física de Partículas, Universidade de Santiago de Compostela, Spain

Magdalena Rafecas
Instituto de Física Corpuscular, Universitat de València /CSIC, Valencia, Spain

Juan Enrique Ortuño, George Kontaxakis, and Andrés Santos
Departamento de Ingeniería Electrónica, Universidad Politécnica de Madrid and CIBER en Bioingeniería, Biomateriales y Nanomedicina (CIBER-BBN), Spain

Javier Pavía
Servei de Medicina Nuclear, Hospital Clínic de Barcelona Institut d'Investigacions Biomédiques August Pí i Sunyer (IDIBAPS) and CIBER en Bioingeniería, Biomateriales y Nanomedicina (CIBER-BBN), Spain

Domènec Ros
Unitat de Biofísica, Facultat de Medicina, Universitat de Barcelona Institut d'Investigacions Biomèdiques August Pí i Sunyer (IDIBAPS) and CIBER en Bioingeniería, Biomateriales y Nanomedicina (CIBER-BBN), Spain

(Received 4 February 2010; revised 22 September 2010; accepted for publication 22 September 2010; published 12 October 2010)

Purpose: In the present work, the authors compare geometrical and Monte Carlo projectors in detail. The geometrical projectors considered were the conventional geometrical Siddon ray-tracer (S-RT) and the orthogonal distance-based ray-tracer (OD-RT), based on computing the orthogonal distance from the center of image voxel to the line-of-response. A comparison of these geometrical projectors was performed using different point spread function (PSF) models. The Monte Carlo-based method under consideration involves an extensive model of the system response matrix based on Monte Carlo simulations and is computed off-line and stored on disk.
Methods: Comparisons were performed using simulated and experimental data of the commercial small animal PET scanner *rPET*.
Results: The results demonstrate that the orthogonal distance-based ray-tracer and Siddon ray-tracer using PSF image-space convolutions yield better images in terms of contrast and spatial resolution than those obtained after using the conventional method and the multiray-based S-RT. Furthermore, the Monte Carlo-based method yields slight improvements in terms of contrast and spatial resolution with respect to these geometrical projectors.
Conclusions: The orthogonal distance-based ray-tracer and Siddon ray-tracer using PSF image-space convolutions represent satisfactory alternatives to factorizing the system matrix or to the conventional *on-the-fly* ray-tracing methods for list-mode reconstruction, where an extensive modeling based on Monte Carlo simulations is unfeasible. © *2010 American Association of Physicists in Medicine*. [DOI: 10.1118/1.3501884]

Key words: 3D PET, iterative reconstruction, list-mode reconstruction, ray-tracing techniques, Monte Carlo simulation, system response matrix

I. INTRODUCTION

Positron emission tomography (PET) allows *in vivo* noninvasive imaging to be applied in diagnostics and basic biomedical research. Nowadays, small animal PET has great potential as a tool in preclinical areas such as drug development, gene expression monitoring, or the development of animal models of diseases.[1–4] Nevertheless, given the difference in size between the small animals used (mice and rats) and humans, the spatial resolution in small animal scanners needs to be considerably improved with respect to human scanners. Furthermore, a similar degree of sensitivity to that found in human studies should be maintained, which is not an easy task if the spatial resolution has to be improved. So, due to these high-resolution and high-sensitivity requirements, both the optimization of PET instrumentation and the development of more accurate reconstruction algorithms are needed.

Analytical reconstruction algorithms (such as filtered backprojection) and iterative reconstruction methods (such as those based on statistical models) are the two major types of tomographic reconstruction methods. Nevertheless, statistical reconstruction methods are becoming a standard procedure in small animal PET due to the possibilities they offer for improved image quality with respect to analytical

methods.[5] The most common statistical reconstruction method is the maximum likelihood expectation maximization[6] and its accelerated version, the ordered subset expectation maximization (OS-EM).[7]

A key element of any statistical reconstruction algorithm is the system response matrix (SRM), which represents the relationship between the image and the projection space. Each element a_{ij} of this matrix corresponds to the probability that a positron emission in voxel j results in the detection of a coincidence event by detector pair i. Therefore, if the original radioactivity distribution in voxel j is represented by q_j and n_i is the statistical noise in the projection, the measured projection p_i can be described by the following equation:

$$p_i = \sum_{j=1}^{J} a_{ij} q_j + n_i, \tag{1}$$

where $i \in [1, I]$, $j \in [1, J]$, and I and J are the total number of lines of response and the total number of image voxels, respectively.

The computation of the elements a_{ij} can be a very laborious task due to the large size of the SRM. To date, several approaches have been developed. To simplify computation and storage, the SRM can be factorized into several submatrices,[8] each one related to a relevant aspect in the image formation process. In this way, the effects of the particular system geometry, the attenuation in the subject, etc., can be calculated separately. While the attenuation matrix can be calculated directly from the attenuation measurements,[9] other effects such as crystal penetration, positron range, intercrystal scatter, or noncollinearity require a more extensive modeling. This modeling can be carried out analytically by using measurements or Monte Carlo (MC) simulations. In any case, the main factor of the SRM is the geometrical component, which accounts for the geometrical efficiency. The elements of this geometrical component are usually calculated analytically, for example, using the Siddon ray-tracer (S-RT).[10] This method is widely used because it is fast and easy to implement. Furthermore, a spatial resolution model can be easily incorporated into this ray-tracer by using image-space convolutions[11,12] so that the projection is modeled as a 3D shift-invariant Gaussian function. Other accurate projectors have recently been proposed: An analytical calculation of the volume-of-intersection (VOI) providing a uniformly continuous sampling of the image space was introduced by Scheins *et al.*[13] Additionally, a new method was presented[14] to accelerate the calculation of VOIs between tubes-of-response (TORs) and voxels based on the Wu-antialiased ray-tracer. These methods yield better images than the Siddon ray-tracer, but more computational effort is needed. A fast and efficient 2D geometrical projector based on MC simulations using image basis functions (only geometrical contributions are computed) has also been proposed.[15] In a previous study,[16] we proposed a geometrical projector, the orthogonal distance-based ray-tracer (OD-RT), based on computing the orthogonal distance from the center of image voxel to the line-of-response (LOR). A similar approach based on the orthogonal distance was also used by Lewitt,[17,18] but in combination with spherically symmetric basis functions (blobs); in a recently published study,[19] the orthogonal distance was used to sample a Gaussian function. The geometrical response matrix can be also derived by measurements[20,21] so that the matrix elements are obtained by positioning the point source in the scanner field of view and processing the response in the projection space (both geometrical and detection physics components are included).

As an alternative to factorization, Monte Carlo simulations can be also used to compute the complete system response model (MC-based SRM).[22–27] Although MC-based SRM methods can improve the image quality by considering almost all image degradation effects, their implementation still remains a challenging computational task. Object scatter could be, in principle, included into the SRM. To date, this approach is seldom used for PET due to its computational complexity.[28] The accurate estimation of object scatter is usually performed before reconstruction, for example, using the single scatter simulation algorithms[29–31] or the double scatter simulation algorithm.[32] The estimated contribution is then included into the forward projection step of iterative algorithms, instead of being within the SRM.

In general, the elements of the SRM can be either computed off-line and stored on disk (MC-based SRM) or calculated during the reconstruction process (*on-the-fly*). The latter approach is suitable for list-mode reconstruction, where the reconstruction process must be performed event by event, and in the modern time-of-flight PET scanners.[33] However, to be efficient, on-the-fly approaches usually only compute the geometrical component of SRM.

The aim of the present work is first to assess in detail the performance of the geometrical OD-RT ray-tracer[16] as an efficient and accurate alternative to the conventional S-RT and then to compare it to a more extensive modeling based on Monte Carlo simulations and more accurate point spread function (PSF) models for geometrical projectors. Both simulated and experimental data from a small animal PET scanner were used for this purpose, with the aim of investigating whether or not the OD-RT method is sufficient for complete SRM modeling. This could be of special interest for list-mode reconstruction.

II. MATERIALS AND METHODS

II.A. Small animal scanner

Our work focuses on the commercial small animal PET scanner *rPET* (Ref. 34) *(Sedecal, Sociedad Espanola de Electromedicina y Calidad S.A.*, Madrid). This scanner is characterized by four opposing planar pixilated detectors with 35 axial $\times$ 30 transaxial LYSO crystals ($1.5 \times 1.5 \times 12$ mm^3). The intrinsic spatial resolution determined by scanning a ^{22}Na point source across its field-of-view (FOV) was 1.5 mm.[34] The axial and transaxial distance between the center of two contiguous crystals is 1.62 mm (including the gap). The radius of the system is 80 mm (i.e., the distance between planar detectors is 160 mm). The width of the coincidence window is 5 ns and the estimated time resolution is 2 ns. The energy window used was 250–650 keV and the

energy resolution is 22%. The sensitivity of the system calculated by using an axial source placed it the center of the FOV was 350 cps (counts per second) per μCi.

II.B. Image reconstruction

For the current work, the statistical iterative reconstruction algorithm, 3D OS-EM-MRP, was implemented. This method is based on the OS-EM algorithm but includes a median root prior (MRP) regularization. MRP regularization is applied in order to control the noise level in the reconstructed images.[35] The median is used as penalty function and it is set for a pixel against the local median so that the penalty is set only if the image is nonmonotonic[36] within the local voxel neighborhood. The reconstructed image is obtained from comparisons between estimated and measured projection data in such a way that each element q_j of the image at iteration $k+1$ for a given subset n is updated according to the following equation:

$$q_j^{k+1,n} = \frac{q_j^k}{s_j^n + \beta U(q^k)} \sum_{i=1}^{I_n} a_{ij} \frac{p_i}{\hat{p}_i^k}. \tag{2}$$

An iteration of OS-EM is thus defined as a single pass through all the subsets, where a_{ij} is an element of the SRM; $i \in [1, I_n]$ is the projection index (or sinogram bin), I_n is the number of projection elements in the subset n ($n \in [1, SB]$, SB is the number of subsets); and $j \in [1, J]$ is the image index, with J being the number of image elements (or voxels);

p_i is the measured projection data; $\hat{p}_i^k$ ($i \in [1, I_n]$) is the estimated projection data for the subset n which is obtained after forward projection of the estimated image at iteration k as

$$\hat{p}_i^k \equiv \sum_{j=1}^{J} a_{ij} q_j^k. \tag{3}$$

$\beta U(q^k)$ is the MRP regularization term, and $U(q^k) = (q_j^k - M_j)/M_j$ is the penalty function, where M_j is the median value obtained considering a window of $3 \times 3 \times 3$ neighborhood voxels. The MRP regularization term is multiplied by a weight factor ($\beta = 0.1$).

s_j^n is an element of the sensitivity image for the subset n, which represents the probability that a positron emission occurred in voxel j was detected and can be obtained by adding only those projection elements within subset n of the SRM according to

$$s_j^n \equiv \sum_{i=1}^{I_n} a_{ij}. \tag{4}$$

Seventeen angular subsets and 170 total iterations were performed, and an image support made of $64 \times 64 \times 69$ voxels with a voxel size of $0.74 \times 0.74 \times 0.8$ mm^3 was used.

II.C. System response matrix calculation

As discussed above, the SRM can be decomposed into several factors in such a way that the geometrical component can be obtained separately. In the present work, the matrix elements a_{ij} were obtained by using two analytical approaches, S-RT and OD-RT, which mainly accounted for geometrical effects. These methods are explained in detail in Secs. II C 1 and II C 2. Figure 1 shows a scheme of the ray-tracing techniques, S-RT and OD-RT. Voxel contributions are represented by levels of gray ranging from white to black. Additionally, the complete SRM was calculated using a Monte Carlo-based method (MC-SRM) (see Sec. II C 3).

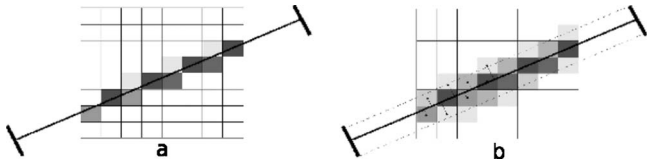

FIG. 1. S-RT (a) and OD-RT (b). The grayscale is proportional to the detection probability of positron emission in various voxels for a given bin. In (a), the probability is calculated as the length of intersection between the LOR and the voxel (S-RT); in (b), as one minus the normalized perpendicular distance from the voxel to the LOR (OD-RT) [see Eq. (5)].

II.C.1. Siddon ray-tracer

The S-RT method is a very widely used technique for computing geometrical efficiencies. Given a projection bin i and a voxel j, the values of a_{ij} are computed as the length of intersection between the LOR related to bin i and voxel j. Thus, each bin is considered to be pointlike, as shown in Fig. 1(a).

II.C.2. Orthogonal-distance ray-tracer

The geometrical OD-RT method calculates each a_{ij} as one minus the normalized orthogonal distance d_{ij} between the voxel center j and the LOR i so that the distance is less than the full width at half maximum (FWHM) of the system PSF. The orthogonal distance d_{ij} is normalized with respect to the FWHM (for this particular PET system, it so happens that the FWHM is equal to the crystal size),

$$a_{ij} = 1 - \frac{d_{ij}}{\text{FWHM}}. \tag{5}$$

The number of voxels to be considered is selected by using a minimum threshold that controls the contribution per voxel. This number is enlarged as the minimum threshold is lowered. Low values of the threshold allow a better modeling of the VOI between voxels and TORs to be computed, but at the cost of increasing the computation time. In this work, the following values for the minimum threshold were studied: 0.5 (OD-RT-5), 0.1 (OD-RT-1), 0.01 (OD-RT-01), and 0.001 (OD-RT-001). Figure 1(b) shows a 2D schematic description of the OD-RT technique.

Given a certain projection bin i, a large part of image voxels will be related to SRM values lower than the threshold. However, the OD-RT method requires the orthogonal distance from all image voxels to each LOR to be computed because the condition $d_{ij} < \text{FWHM}$ has to be checked. In order to speed up the OD-RT method, a more efficient way

of computing the elements of SRM was implemented so that the neighbors that can have a weight above the minimum threshold are deterministically found. First, the Siddon ray-tracer was used to find those voxels that are crossed by the LOR. The orthogonal distances are then computed only from these voxels and from their adjacent voxels. If the weights obtained are greater than the threshold value, the orthogonal distances are computed from the voxels adjacent to the previous voxels. The process continues until the weight obtained for each adjacent voxel is lower than the threshold value or the orthogonal distance is larger than FWHM.

II.C.3. Monte Carlo-based SRM

For the sake of comparison, we also implemented the custom MC reconstruction method presented in Refs. 25 and 37, where the SRM is calculated by using MC techniques to estimate the probabilities for every sinogram bin. In this study, this MC-based SRM model was used as a reference for comparison.

The implemented in-house MC code is based on the generation of a high number of annihilation events for every voxel located in the FOV (10^8 photons per voxel), excluding the voxels whose SRM values can be calculated using symmetries. The results obtained from the simulation of each voxel represent a SRM column, or, equivalently, a projection set, represented as a set of plane and oblique sinograms. In every event, a pair of simulated gamma rays is generated uniformly only within the solid angle of coincidence, which is relatively small in rPET scanner geometry. Gantry rotation is modeled with uniformly distributed complementary rotation of sources.

The photon tracking has been modeled using the National Institute of Standard and Technology (NIST) photon cross-section tables.[38] The total cross section is the sum of the photoelectric, pair production, coherent, and incoherent (Compton) scattering, but only Compton and photoelectric effects are significant at 511 keV. Compton iterations are modeled by sampling the Klein–Nishina distribution. A variation in the Kahn double-rejection technique is used for sampling the scattered photon energy and the scattering angle.[39] The number of allowed scatters and the minimum energy can be limited to speed up the process. Noncollinearity effects are modeled with a Gaussian distribution of 0.5 degrees. Positron range is modeled with the sum of two exponentials[40] that are sampled in the MC code with the accept-reject algorithm. Crystal penetration and intercrystal scatter were also simulated.

Variance reduction techniques are employed in order to obtain better statistics. These techniques are applied to the gamma ray tracking in the detector with an auxiliary lookup table, where probabilities of detection in the neighboring crystals were stored according to the angle and relative point of intersection with the detector.

Simulation results were directly processed and stored in sparse-mode matrix format. Once the simulation is completed, data are postprocessed to distribute SRM values between the selected numbers of subsets. The simulation time was 18.4 h and 1206 mean coincidences per LOR were detected.

II.D. PET data

II.D.1. Simulated data

In order to simulate PET data, we used MC simulations, a versatile tool that is considered to be the gold standard to assess reconstruction algorithms and the quantification outputs. This methodology allows us to evaluate the algorithms in a realistic and well controlled framework in which all the parameters are known *a priori*. The rPET system was described using SimSET v2.6.[41,42] Thus, all phantom simulations were carried out including scatter, absorption, positron range, and noncollinearity. The positions of the interactions within the layers of the planar detector were processed to compute the centroid and the total deposited energy. Photon interactions including scatter, absorption, and penetration were simulated, but there are no blocks and hence no gap effects. Scintillation photons and photomultiplier tubes were not simulated and the detector was modeled with an ideal time resolution.

Two cylindrical phantoms (diameter: 25 mm) were simulated: A hot-cylinder phantom (HCP) with six hot axial cylinders placed in water without any activity (radii: 1, 2, 3, 4, 5, and 6 mm; volume: 173, 693, 1560, 2774, 4335, and 6242 mm^3). As a general rule, cold rods on an active background represent a more challenging reconstruction problem than hot rods. Therefore, simulations using the same geometrical distribution were also undertaken with cold rods on an active background [cold-cylinder phantom (CCP)]. The number of acquired counts was 189 million counts for HCP and 116 million counts for CCP. PET data were histogrammed and stored in 3D sinograms characterized by 59 transaxial bins (axial and transaxial bin size: 0.81 mm) and 170 angular positions, with no axial or angular compression (span=1 and mashing=1) to preserve spatial resolution.

II.D.2. Experimental data

A custom-made micro-Derenzo hot rod phantom was used for a qualitative study of the spatial resolution. This phantom had a diameter of 25 mm and contained fillable hot rods of 1 mm in diameter arranged in six circular sectors. The air spacings between rods (center to center distance) in each circular sector were 2, 3, 4, 5, 6, and 8 mm, respectively. The number of acquired counts was 93 million counts.

A spiral phantom was used for a quantitative study of the spatial resolution. This phantom contained fillable capillaries of 0.3 mm in diameter placed at different distances from the axial axis of the system (2.8, 9.4, 10.0, 12.2, 14.0, 17.0, and 19.0 mm) and they were arranged in a spiral configuration. The hot rods and the capillaries were filled with ^{18}F-FDG and scanned on the rPET system, and 133 million counts were acquired.

As for the simulated data, the measured data were stored in 1225 sinograms characterized by 59 transaxial bins (axial

and transaxial bin size: 0.81 mm) and 170 angular positions. Axial positions were not added (span=1) and no mashing was considered (mashing=1).

II.E. Evaluation

II.E.1. Sensitivity images

The sensitivity images were analyzed to study the ability of the approach based on the OD-RT method compared to the conventional S-RT method to model the system response. To this end, tangential profiles through the center of the central slice of these sensitivity images were obtained for the different geometrical projectors. The theoretical profile was calculated from the angle subtended at each voxel along the transaxial direction.

The profiles of the sensitivity images were also obtained in order to evaluate the performance of the different PSF models for S-RT and OD-RT. Both the multiray and the image-space convolution techniques were evaluated in terms of these sensitivity images.

For comparison, sensitivity profiles for MC-SRM were also obtained by simulating a high number of events for every voxel located along the transaxial direction of the FOV. The voxels whose probability coefficients can be calculated using symmetries were excluded, i.e., only the voxels placed between the center and the perimeter of the FOV were considered.

II.E.2. Correlation coefficient

Correlation coefficients (CCs) were calculated between the reconstructed image and the simulated phantoms (HCP and CCP) according to Eq. (6),

$$\mathrm{CC}=\frac{\sum_{j=1}^{J} q_j q_j^{\mathrm{ref}} - J^2(\bar{q}\cdot\bar{q}^{\mathrm{ref}})}{\sqrt{\sum_{j=1}^{J} q_j^2 - J^2\bar{q}^2}\sqrt{\sum_{j=1}^{J}(q_j^{\mathrm{ref}})^2 - J^2(\bar{q}^{\mathrm{ref}})^2}}, \tag{6}$$

where $\bar{q}$ represents the mean value of the reconstructed image, J is the number of image voxels, and q_j is the image value in voxel j. The superscript ref refers to the values obtained from the reference image (simulated phantom). The values of CC should be in the interval [0,1], and ideally, CC=1. The inter-iteration relative variation (δCC) in CC values between iteration i and iteration $i-1$ was also obtained in order to study the convergence of each reconstruction method in terms of CC.

II.E.3. Contrast

The contrast (C) was obtained for HCP and CCP according to the following equation:

$$C=\frac{\bar{q}_{\mathrm{ROI}}-\bar{q}_{\mathrm{bg}}}{\bar{q}_{\mathrm{ROI}}+\bar{q}_{\mathrm{bg}}}, \tag{7}$$

where $\bar{q}_{\mathrm{ROI}}$ is the mean value in a region-of-interest (ROI) drawn within the cylinders and $\bar{q}_{\mathrm{bg}}$ is the mean value of the background. These ROIs, which have volumes of 8.7, 9.0, 28.5, 46.0, 70.1, and 102.9 mm^3, spread over five contiguous axial slices. The volume of background ROI was 1612 mm^3 and was also extended in five contiguous axial slices. In an ideal reconstruction, C should be 1 for HCP and -1 for CCP.

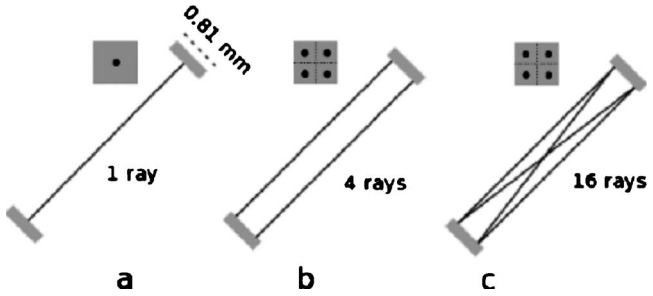

FIG. 2. A 2D description of different multiray schemes and the subsampled bins for S-RT, the conventional Siddon approach (a), subsampled 4 parallel rays, S-RT-SS4 (b), and subsampled 16 parallel and crossed rays, S-RT-SS16 (c).

The C recovery was defined as the relation between the calculated and the theoretical contrast (in %). The C recovery was obtained by using the abovementioned ROIs, but drawn in ten blocks of five contiguous slices placed at different axial positions along the image. This procedure allowed us to assess the statistical significance of the results. In order to compare C values at the optimal number of iterations in each case, the inter-iteration variation (δC) between C values was obtained at consecutive iterations i and $i-1$.

II.E.4. Coefficient of variation

To assess the impact of the projector on image noise, the coefficient of variation (CV) was obtained for CCP. This parameter was defined as the ratio between the standard deviation and the mean value of the voxels in a ROI. CV was determined as the mean value of the CV computed in ROIs placed close to the center of CCP (homogeneous region).

II.E.5. Evaluation of the PSF models

An assessment of different PSF models for S-RT and OD-RT was also carried out to ensure a more fair head-to-head comparison between geometrical projectors and the extensive model of SRM based on MC simulations.

II.E.5.a. Multiray Siddon ray-tracer (S-RT-SS). To include the detector size in the model, we have modified the conventional S-RT method so that several rays were traced for each crystal. The crystal was subsampled (SS) into four equal units in the axial and transaxial directions. In this way, TORs were considered instead of LORs. Within this subsampling, we implemented two ray-tracing schemes, one including only 4 rays (only parallel lines, S-RT-SS4) and another including 16 rays (parallel and crossed lines, S-RT-SS16) per bin. A 2D schematic description is shown in Fig. 2. It should be noted that for a given i, more voxels are included in the SRM estimation using the subsampled techniques than the conventional S-RT. Finer subsampling of the crystal size was not performed (for example, into 9 or 16 equal units) due to

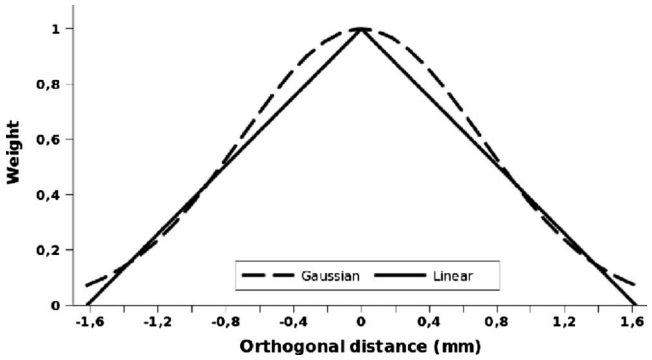

FIG. 3. Modeling of the intrinsic detector response by sampling a linear function (solid line) and a Gaussian blurring (dashed line).

the significant increase in computing time. (Long computation times are against the rationale behind fast ray-tracing techniques such as S-RT.)

II.E.5.b. Siddon ray-tracer using PSF image-space convolutions (S-RT-PSF). The conventional S-RT method can also be implemented, incorporating a PSF model based on image-space convolutions.[11,12] Thus, the projection was modeled as a 3D Gaussian convolution of the image, followed by the conventional S-RT, and backprojection as S-RT, followed by convolution. A shift-invariant Gaussian reconstructed point response function with FWHM equal to the crystal size was included (although wider kernels were also tested). Apart from the convolution of the sensitivity image, two convolution operations were implemented, corresponding to the system matrix for the forward model and the transpose of the system matrix.

II.E.5.c. Orthogonal-distance ray-tracer using a Gaussian kernel (OD-RT-G). The OD-RT method already incorporates a built-in PSF model based on a linear kernel, which could be a good approach to the spatial resolution of the system. Nevertheless, we also implemented a kernel based on Gaussian functions (OD-RT-G), as proposed in Ref. 19. Figure 3 shows the resulting intrinsic detector responses by sampling a linear function and a Gaussian function. The FWHM for the implemented Gaussian function was equal to the crystal size (although wider kernels were also tested), making it consistent with the previous linear function.

II.E.6. Spatial resolution

Spatial resolution was obtained by using a spiral phantom including axial capillaries at different distances from the center (0, 2.8, 4.8, 9.4, 10.0, 12.2, 14.0, 17.0, and 19.0 mm).

II.E.7. Time and memory requirements

In list-mode reconstruction, SRM elements are computed on-the-fly, especially the geometrical component, and therefore, a full estimation of the SRM using a Monte Carlo-based method would result in impractically long computing times (18.4 h). Aimed at studying the feasibility of using the implemented ray-tracers (subsample S-RT, S-RT-PS,F and OD-RT) for list-mode reconstruction, the computational requirements of these methods were investigated in terms of time and memory.

III. RESULTS

III.A. Evaluation of the system response matrix calculation

III.A.1. Sensitivity images

The profiles of the sensitivity images obtained using OD-RT-5, OD-RT-1, OD-RT-01, and the conventional S-RT method are shown in Fig. 4. Very jagged profiles were obtained using the conventional S-RT. Nevertheless, it can be seen that low minimum thresholds in OD-RT lead to a better

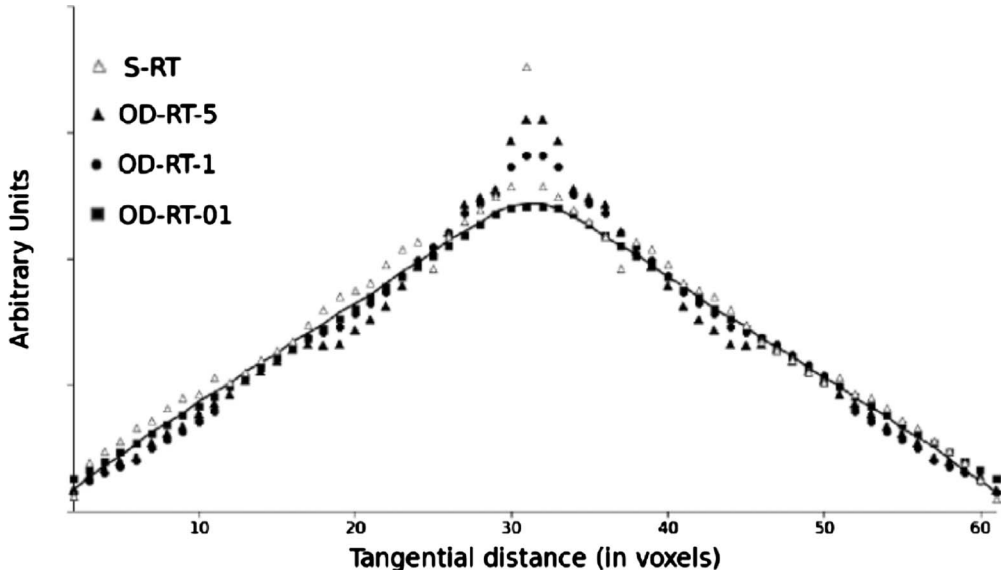

FIG. 4. Tangential profiles through the sensitivity images obtained by using S-RT (hollow triangles), orthogonal distance-based ray-tracer for minimum thresholds of 0.5 (filled triangles), 0.1 (filled circles), and 0.01 (filled squares). The solid line is the theoretically calculated curve.

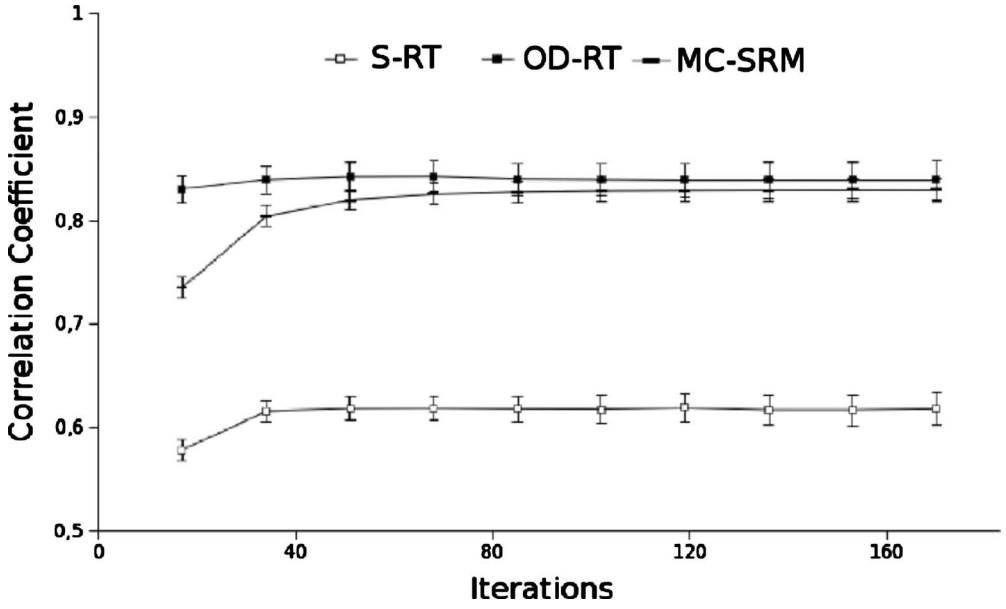

FIG. 5. Iteration-dependence of CC for images reconstructed using a SRM based on the Siddon ray-tracer (hollow squares), OD-RT-01 (filled squares), and MC-SRM (small segment) methods for the CCP reconstructions.

modeling (artifact-free). OD-RT sensitivity maps obtained for minimum thresholds of 0.5 (OD-RT-5) and 0.1 (OD-RT-1) were affected by overestimation of the sensitivity at the center and jagged profiles, both of which are common artifacts when using ray-tracing techniques such as S-RT. On the contrary, using a minimum threshold of 0.01 (OD-RT-01) removed the sensitivity overestimation at the central voxels and showed the desired smooth profiles, which were similar to those estimated using theoretical calculations. A tangential profile was also obtained by using a minimum threshold of 0.001 (OD-RT-001). This resulted in a profile very similar to that obtained by using a minimum threshold of 0.01; therefore, the latter has been omitted for clarity.

III.A.2. OD-RT versus S-RT and MC-SRM

Figure 5 shows the iteration dependence of CC [see Eq. (6)] for images of CCP reconstructed using a SRM based on the S-RT, OD-RT-01, and MC-SRM methods. Given that a MRP regularization was used, CC reaches a stable value after a certain number of iterations. Similar behavior was found for HCP.

The improvement of CC lies below 1% after iteration 34 for OD-RT-01, after iteration 64 for S-RT, and after iteration 66 for MC-SRM. Interestingly, the convergence is faster for OD-RT than for S-RT and MC-SRM (in terms of CC). Similar behavior was found for HCP, although in this case stable CC values were achieved before iteration 17 for all methods. In order to ensure that the comparison of methods was performed in similar conditions, the number of iterations required to stabilize CC was used for each method and phantom.

As for OD-RT, our findings show that a lower threshold results in a higher CC value. Thus, CC increased from 0.91 for OD-RT-5 to 0.94 for OD-RT-01 when HCP was used, and from 0.76 for OD-RT-5 to 0.84 for OD-RT-01 when CCP was used. The reason is that, for a given detector pair, more voxels are included in the SRM estimation when the minimum threshold decreases so that a better approximation of the true volume of intersection is achieved. No differences were found in terms of CC between OD-RT-01 and OD-RT-001. In any case, the most significant result was that the OD-RT technique yielded much higher values of the correlation coefficient than the S-RT method, both for HCP (CC increases by 16%) and CCP (CC increases by 35%).

Transverse views of the reconstructed images (for HCP and CCP) obtained by using the conventional S-RT, OD-RT-01, and MC-SRM are shown in Fig. 6. The number of iterations corresponded to the number of iterations required to stabilize CC for all method and phantoms (66 for CCP and 17 for HCP). For HCP, we can observe that the three reconstructed images are very similar, while notable differences are appreciable in CCP. In the latter case, the use of OD-RT-01 proved to be a significant improvement on the S-RT method. As expected, the MC-SRM yielded the best image.

The contrast (C), as defined in Eq. (7), was calculated for HCP and CCP. The optimal number of iterations for comparing contrast values is usually object-dependent, and therefore, convergence is not reached at the same iteration. Thus, an appropriate number of iterations were determined for each phantom by comparing the inter-iteration variation in the contrast (δC) obtained for one of the cold cylinders (radius: 4 mm). The comparison shows that at least 85 iterations are required to ensure convergence (beyond 85 iterations, the differences between consecutive C values were less than 1% for S-RT and MC-SRM). It should be noted that a faster convergence of the OD-RT in terms of contrast was found (beyond 52 iterations, δC values were less than 1%). Given that hot regions (HCP) are easier to reconstruct correctly

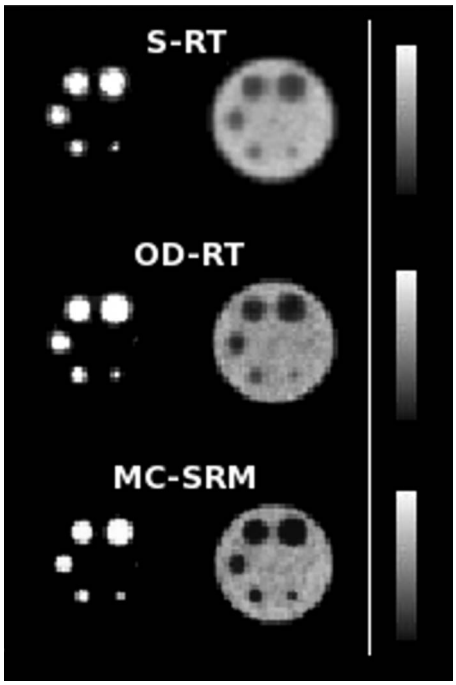

FIG. 6. Transverse views of the reconstructed images from HCP (left) and CCP (right) using a SRM obtained by using the S-RT (upper row), OD-RT-01 (middle row), and MC-SRM (lower row).

than cold regions (CCP), the convergence of HCP reconstruction was already ensured after 34 iterations for all methods. Therefore, images employed in this contrast analysis were reconstructed using 85 iterations for CCP and 34 iterations for HCP.

The CV was also obtained in order to make sure that the comparison between algorithms is performed at an equivalent noise level. CV was obtained from the CCP reconstructions by using 85 iterations. It was 4.7% for the S-RT method, 4.9% for the OD-RT-01 method, and 4.4% for the MC-SRM method. These results ensure that the images used in the comparison show a similar noise level.

Figures 7(a) and 7(b) show that C recovery increases with the diameter of cylinder. As for HCP, Fig. 7(a) shows that higher C recovery values were obtained for the OD-RT-01 and MC-SRM methods than for the S-RT method. This relative improvement is larger for the small cylinders. A similar behavior was found in the CCP reconstructions. Figure 7(b) shows that higher C recovery values were obtained for the OD-RT-01 and MC-SRM methods. A paired t-test was performed in order to determine if these results were statistically significant ($p<0.05$).

As for HCP, significant differences in C recovery were found between OD-RT-01 and S-RT ($p=2E-5$ and the mean difference observed in C recovery was 6.3%). Moreover, the smallest cylinder (radius: 1 mm) could not even be distinguished from the background (C recovery around zero) in the S-RT reconstructions. On the other hand, no significant differences between MC-SRM and OD-RT-01 were found.

As for CCP, the comparison between OD-RT-01 and S-RT resulted in significant differences again ($p=1E-24$ and the mean difference observed in C recovery was 9.4%). Unlike HCP, significant differences were found between MC-SRM and OD-RT, although the mean difference was low ($p=6E-3$ and the mean difference observed in C recovery was only 1.2%).

Concerning OD-RT, the choice of the minimum threshold is a key issue in order to obtain high C values. Thus, the obtained C recovery for the smallest rod in HCP was 0.4% for OD-RT-5, 24% for OD-RT-1, and 55% for OD-RT-01. Again, no differences were found between OD-RT-01 and OD-RT-001. It should be noted that higher C recovery values were obtained from HCP than from CCP.

III.B. Evaluation of the PSF models

Different PSF models for S-RT and OD-RT were also assessed so as to make a fairer head-to-head comparison between geometrical and Monte Carlo projectors. This evaluation was carried out by using real data in order to uncouple the possible mismatch between the simulated data and the simulation code used to generate the SRM due to the fact that the physical model in MC-SRM is actually very realistic and includes more phenomena than the simulated data. An evaluation of the ability of these approaches to model the system response in terms of sensitivity images was carried out. In order to obtain qualitative and quantitative results of the spatial resolution, real studies of a micro-Derenzo phantom and a spiral phantom (axial capillaries arranged in a spiral configuration) were also performed.

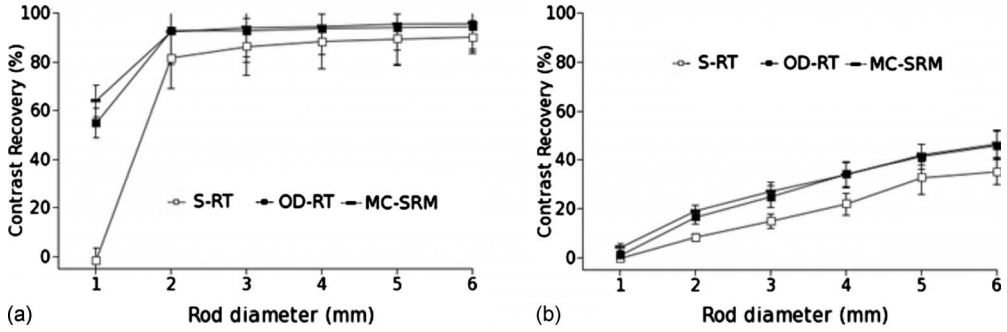

FIG. 7. Contrast recovery obtained by means of the S-RT (hollow squares), the OD-RT-01 (filled squares), and MC-based SRM (small segment) for each axial cylinder of HCP (a) and CCP (b).

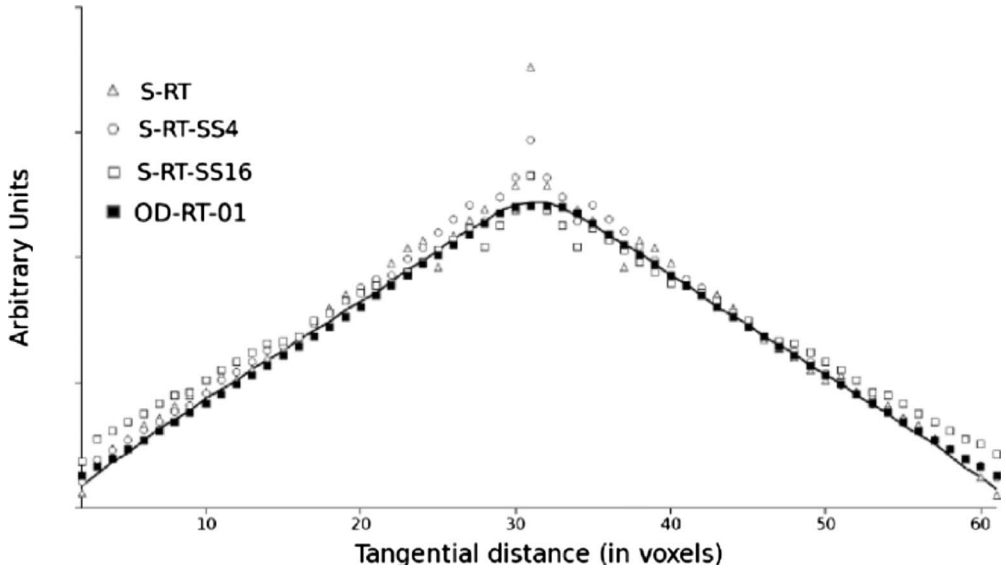

FIG. 8. Tangential profiles through the sensitivity images obtained by using S-RT (hollow triangles), subsampled S-RT (hollow circles for 4 rays per detector, and hollow squares for 16 rays per detector), and OD-RT-01 (filled squares). The solid line is the theoretically calculated curve. Profiles for MC-SRM and S-RT-PSF resembled the theoretical profiles so are not shown.

III.B.1. Sensitivity images

The profiles of the sensitivity images obtained from S-RT, S-RT-SS4, S-RT-SS16, OD-RT-01, and the theoretical profile are shown in Fig. 8. Sensitivity profiles obtained for MC-SRM and S-RT-PSF resembled the theoretical profiles and so they are not shown (they are very close to the OD-RT-01 profile and for reason of clarity were not plotted). It should be noted that jagged profiles of the sensitivity maps were obtained using S-RT, and the subsampling of the detectors (4 and 16 rays) improved the results with respect to the original S-RT. This is due to the fact that multiray schemes approximate the detector size by subsampling the detector into four equal units in the axial and transaxial directions.

III.B.2. Micro-Derenzo phantom

Figure 9 compares transverse slices of the reconstructed image from the home-made micro-Derenzo phantom acquisition using the Siddon approaches (S-RT, S-RT-SS4, S-RT-SS16, and S-RT-PSF), OD-RT methods (OD-RT-01 and OD-RT-01-G), and MC-SRM method. All images were obtained after 68 iterations. The comparison shows that all the hot rods spaced at 4, 5, 6, and 8 mm can be clearly identified on all images; however, the hot rods spaced at 3 mm can only be clearly distinguished on images reconstructed by the geometrical projectors with PSF models and Monte Carlo projector. Moreover, a nonzero background is observed in the central part of the reconstructed images by the conventional S-RT, which could be due to the artifacts of the sensitivity image shown in Fig. 4. If they are iterated beyond 68 iterations, these artifacts increase. The comparison also shows that the hot rods spaced at 2 mm can only be identified on images reconstructed by S-RT-PSF, OD-RT, OD-RT-GT, and MC-SRM. This could be due to the fact that these methods not only take into account the size of the detector but also include a better approach to the computation of detector response.

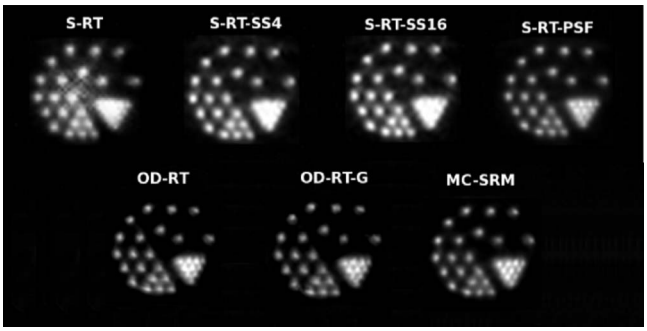

FIG. 9. Reconstructed images from experimental home-made micro-Derenzo phantom using, from left to right, S-RT, S-RT-SS4, S-RT-SS16 and S-RT-PSF (top), and OD-RT-01, OD-RT-01-G, and MC-based SRM (bottom).

III.B.3. Spiral phantom: Spatial resolution measurements

The averaged spatial resolution values (FWHM in mm) at different distances and the standard deviation were obtained using the conventional S-RT, S-RT-SS4, S-RT-SS16, and the S-RT method, incorporating an approximate PSF model (S-RT-PSF). Table I shows these results compared to the spatial resolution values obtained by OD-RT-01, OD-RT-01-G, and MC-SRM methods. The averaged spatial resolution values corresponded to the minimum values along the iterations for each method. The minimum spatial resolution for S-RT, S-RT-SS4, S-RT-SS16, S-RT-PSF, and OD-RT-01-G was obtained after 102 iterations, and for OD-RT-01 and MC-SRM after 85 iterations. The low standard deviation values show that no major differences were found between the different

TABLE I. Averaged spatial resolution and standard deviation.

Projector	FWHM (mm)	Standard deviation (mm)
S-RT	1.83	0.02
S-RT-SS4	1.76	0.04
S-RT-SS16	1.62	0.04
S-RT-PSF	1.39	0.17
OD-RT-01-G	1.42	0.05
OD-RT-01	1.40	0.10
MC-SRM	1.21	0.09

distances from the axial axis of the system (0, 2.8, 4.8, 9.4, 10.0, 12.2, 14.0, 17.0, and 19.0 mm with standard deviation values less than 0.2 mm in all cases). No differences were found when wider kernels for the OD-RT and S-RT-PSF models were used.

It should be mentioned that an assessment of the spatial resolution from point source measurements in air is challenging and it can lead to unreal results when broader-than-real PSF and small pixels are used.[43] These spatial resolution values can be considered as useful relative measurements for the comparison, but the limitation of this metric should be taken into account if these values are considered as measurements of the spatial resolution of the system.

Table I shows that spatial resolution was enhanced when using OD-RT-01 and S-RT-PSF compared to conventional and multiray geometrical projectors (S-RT-SS16: $p<0.05$). Similar averaged spatial resolution values were obtained by using the Gaussian kernel (OD-RT-01-G) compared to the values obtained by using OD-RT-01 and the S-RT-PSF methods.

One explanation as to why spatial resolution is enhanced when using OD-RT, compared to conventional S-RT, is that the OD-RT method incorporates a coarse model for the intrinsic detector response. As shown in Fig. 3, a triangular function can result in a good approach for the more realistic Gaussian-based modeling of the detector response with FWHM equal to the crystal size. The latter leads to a detector response function, which has a maximum at the center of the TOR and decreases linearly to zero at a distance $2BS$, and this triangular function or linear kernel models the intrinsic spatial resolution at the midplane for opposed detectors.[44] A similar explanation can be derived for the S-RT-PSF method because it incorporates a shift-invariant Gaussian reconstructed point response function with FWHM equal to the crystal size.

Although multiray Siddon techniques take into account the size of the detector, our results show that the modeling of the intrinsic detector response using this method does not seem a good approach. The multiray techniques apply subsampling within a single detector, but this is not a realistic model of the PSF. A comparison[13] between a ray-tracer method based on the conventional Siddon ray-tracer and an analytical calculation of VOIs between TORs and voxels supported the hypothesis that an analytical calculation of VOI systematically provides higher contrast recovery values. Thus, the implementation of a very high level of subsampling could improve the performance of S-RT but it would be too slow and impractical (computation time is approximately proportional to the number of rays traced).

Unlike the simulated data, the image of MC-SRM method was clearly better than the image of S-RT-PSF and OD-RT methods, and significant differences ($p<0.05$) were found between spatial resolution values. At this point, it should be mentioned that the simulations of the phantoms do not include either crystal penetration or intercrystal scatter, while both these two effects are included in the simulations for the SRM. In any case, both geometrical OD-RT and S-RT-PSF methods result in a fairly accurate approach when compared to the conventional S-RT.

TABLE II. Computation time on an Intel(R) Xeon(TM) CPU 3.20 GHz dual-processor and SRM size per subset (Mb).

Projector	Events per second	Size per subset (Mb)
S-RT	47 200	355
S-RT-SS4	10 634	936
S-RT-SS16	2 389	945
S-RT-PSF	47 200	355
OD-RT-5	6 045	832
OD-RT-1	5 480	953
OD-RT-01	4 980	1065
OD-RT-01-G	4 681	1067

III.C. Time and memory requirements

Table II presents the number of events per second that could be projected in a list-mode reconstruction scheme for different S-RT and OD-RT methods on an Intel(R) Xeon(TM) CPU 3.20 GHz dual processor. Table II also shows the size of the SRM per subset (in Mb).

As seen in Table II, multiray Siddon techniques (S-RT-SS4 and S-RT-SS16) resulted in an increase in the computation time compared to the conventional S-RT (by factors of 4.5 and 20, respectively). In a list-mode reconstruction scheme, where SRM is computed on-the-fly, a typical acquisition of 70 million events would lead to computation times of 25, 110, and 488 min when using S-RT, S-RT-SS4, and S-RT-SS16, respectively. Multiray-based schemes based on more than 16 rays were also studied, but they resulted in computation times much longer than those required for OD-RT.

Table II also shows that the choice of minimum threshold in OD-RT also affected computation time. It should be noted that fewer events per second can be projected when the minimum threshold is increased. Additionally, minimum thresholds lower than 0.01 only increased the computation time without adding new information; this can be seen in the size of the SRM size per subset, which is 1065 Mb for OD-RT-001 and OD-RT-01. In a list-mode reconstruction scheme, the processing of 70 million acquired events required 192, 212, and 234 min using OD-RT-5, OD-RT-1, and OD-RT-01, respectively. Furthermore, including the Gaussian modeling

resulted in a minor increase in the computation time with respect to the OD-RT based on linear functions.

The S-RT-PSF method is very fast in comparison to OD-RT-01 and the number of projected events per second is equal to those projected using S-RT. It constitutes only a small increase in the computation time compared to S-RT because only image convolutions per iteration are added during the reconstruction process. We can therefore conclude that both OD-RT-01 and S-RT-PSF can be considered to be satisfactory alternatives to conventional ray-tracers for list-mode reconstruction.

IV. DISCUSSION AND CONCLUSIONS

In this work, we have assessed the effect on the final reconstructed image of different geometrical and Monte Carlo projectors and PSF models used during the reconstruction process. We have compared the conventional Siddon ray-tracer, new subsample techniques for the Siddon ray-tracer, Siddon ray-tracer using PSF image-space convolutions, the recently proposed orthogonal distance-based ray-tracer (using linear and Gaussian kernels), and the Monte Carlo-based method.

Our findings show that the subsample techniques employed, together with the Siddon ray-tracer method, resulted in a behavior similar to that of the conventional Siddon ray-tracer, and only slight improvements were found. The implementation of a very high level of subsampling could improve the performance of S-RT, but it has been shown that it would be impractical because the computation time is approximately proportional to the number of rays traced.

The orthogonal distance-based ray-tracer method yielded better images than those obtained by using the conventional Siddon ray-tracer. An evidence for this is the higher correlation with the original distribution and a significant improvement in contrast and spatial resolution. Furthermore, it has been shown that the correct choice of minimum threshold in the orthogonal distance-based ray-tracer method is crucial for obtaining high quality images.

We also compared the orthogonal distance-based ray-tracer method to the Siddon ray-tracer including PSF image-space convolutions. Our results showed that the built-in resolution model included in the orthogonal distance-based ray-tracer method is equivalent to the conventional S-RT incorporating a PSF model in the image space.

These geometrical projectors were also compared to a more extensive modeling based on Monte Carlo simulations. The latter, as expected, provided superior results (although the quality of the images reconstructed using OD-RT and S-RT-PSF was not significantly poorer). No significant differences were found when kernels wider than FWHM were used to include the nonmodeled effects into the OD-RT and S-RT-PSF methods. This could be due to the fact that these nonmodeled effects can elicit a spatially variant response or even a non-Gaussian response function. However, both the linear kernel and the shift-invariant Gaussian function used in OD-RT and S-RT-PSF model only the intrinsic response function at the midplane for opposing detectors, but do not model the other components of the intrinsic detector response, such as crystal penetration (parallax error), the positioning error due to light spreading, and the intrinsic resolution of the photodetectors.

Multiray-based schemes and the orthogonal distance-based ray-tracer method resulted in an increase in computation time with respect to the conventional Siddon ray-tracer. In this regard, Siddon ray-tracer using a PSF image-space convolution is a better option to include an approximate PSF model because these operations constitute only a small increase in the computation time.

Finally, owing to the improvement in image quality, both orthogonal distance-based ray-tracer and Siddon ray-tracer using PSF image-space convolutions represent satisfactory alternatives to factorizing the system matrix or to the conventional on-the-fly ray-tracing methods for list-mode reconstruction, where an extensive modeling based on MC simulations is unfeasible.

ACKNOWLEDGMENTS

This work was supported in part by Fondo de Investigaciones Sanitarias del Instituto de Salud Carlos III (Project Nos. PI041017, PS09/01206, and CB06/01/1039), by the Ministerio de Ciencia e Innovacion (Grant No. TEC2007-61047), by the Generalitat Valenciana (Grant No. GV06/246), by the Generalitat de Catalunya (Grant No. SGR1049), Ministerio de Ciencia e Innovacion (Project No. SAF2009-08076), and by Ministerio de Ciencia e Innovacion (CDTI-CENIT) AMIT project and Comunidad de Madrid (project ARTEMIS P2009/DPI-1802). P. Aguiar was awarded a "Sara Borrell" fellowship by Fondo de Investigaciones Sanitarias del Instituto de Salud Carlos III.

[a]Electronic mail: pablo.aguiar.fernandez@sergas.es

[1]A. Chatziioannou, "Molecular imaging of small animals with dedicated pet tomographs," Eur. J. Nucl. Med. Mol. Imaging **29**(1), 98–114 (2002).
[2]A. Jacobs, H. Li, A. Winkeler, R. Hilker, C. Knoess, A. Rueger, N. Galldiks, B. Schaller, J. Sobesky, and L. Kracht, "PET-based molecular imaging in neuroscience," Eur. J. Nucl. Med. Mol. Imaging **30**(7), 1051–1065 (2003).
[3]J. Lewis, S. Achilefu, J. Garbow, R. Laforest, and M. Welch, "Small animal imaging: Current technology and perspectives for oncological imaging," Eur. J. Cancer **38**(16), 2173–2188 (2002).
[4]R. Myers, "The biological application of small animal PET imaging," Nucl. Med. Biol. **28**(5), 585–593 (2001).
[5]T. Frese, N. Rouze, C. Bouman, K. Sauer, and G. Hutchins, "Quantitative comparison of FBP, EM and Bayesian reconstruction algorithms for the IndyPET scanner," IEEE Trans. Med. Imaging **22**(2), 258–276 (2003).
[6]L. A. Shepp and Y. Vardi, "Maximum-likelihood reconstruction for emission tomography," IEEE Trans. Med. Imaging **1**, 113–122 (1982).
[7]H. Hudson and R. Larkin, "Accelerated image reconstruction using ordered subsets of projection data," IEEE Trans. Med. Imaging **13**(4), 601–609 (1994).
[8]J. Qi, R. Leahy, A. Chatziioannou, S. Cherry, and F. Farquhar, "High-resolution 3D Bayesian image reconstruction using the microPET small animal scanner," Phys. Med. Biol. **43**(7), 1001–1013 (1998).
[9]H. Zaidi and B. Hasegawa, "Determination of the attenuation map in emission tomography," J. Nucl. Med. **44**, 291–315 (2003).
[10]X. Wu, "An efficient anti-aliasing technique," ACM Computer Graphics Siggraph **25**(4), 143–152 (1991).
[11]A. J. Reader, P. J. Julyan, H. Williams, D. L. Hastings, and J. Zweit, "EM algorithm system modeling by image-space techniques for PET reconstruction," IEEE Trans. Nucl. Sci. **50**, 1392–1397 (2003).
[12]F. C. Sureau, A. J. Reader, C. Comtat, C. Leroy, M. J. Ribeiro, I. Buvat,

and R. Trebossen, "Impact of image-space resolution modeling for studies with the high-resolution research tomograph," J. Nucl. Med. **49**(6), 1000–1008 (2008).
[13]J. Scheins, F. Boschen, and H. Herzog, "Analytical calculation of VOI for iterative fully 3D PET reconstruction," IEEE Trans. Med. Imaging **25**(10), 1363–1368 (2006).
[14]C. Schretter, "A fast tube of response ray-tracer," Med. Phys. **33**(12), 4744–4748 (2006).
[15]S. Vandenberghe, S. Staelens, C. Byrne, E. Soares, I. Lemahieu, and S. Glick, "Reconstruction of 2D PET data with Monte Carlo generated system matrix for generalized natural pixels," Phys. Med. Biol. **51**, 3105–3125 (2006).
[16]P. Aguiar, M. Rafecas, C. Falcon, J. Pavia, and D. Ros, "Fully 3D PET iterative reconstruction using a pseudo-Wu ray-tracer," International Meeting on Fully 3D Image Reconstruction in Radiology and Nuclear Medicine Conference Record, pp. 402–405, 2007 (unpublished).
[17]R. Lewitt, "Multidimensional digital image representations using generalized Kaiser-Bessel window functions," J. Opt. Soc. Am. A **7**(10), 1834–1846 (1990).
[18]R. Lewitt, "Alternatives to voxels for image representation in iterative reconstruction algorithms," Phys. Med. Biol. **37**(3), 705–716 (1992).
[19]G. Pratx, G. Chinn, P. Olcott, and C. Levin, "Fast, accurate and shift-varying line projections for iterative reconstruction using the GPU," IEEE Trans. Med. Imaging **28**(3), 435–445 (2009).
[20]V. Y. Panin, F. Kehren, C. Michel, and M. Casey, "Fully 3-D PET reconstruction with system matrix derived from point source measurements," IEEE Trans. Med. Imaging **25**(7), 907–921 (2006).
[21]A. Alessio, P. Kinahan, and T. Lewellen, "Modeling and incorporation of system response functions in 3D whole body PET," IEEE Trans. Med. Imaging **25**(7), 828–837 (2006).
[22]M. Rafecas, B. Mosler, M. Dietz, M. Pogl, A. Stamatakis, D. McElroy, and S. Ziegler, "Use of Monte Carlo-based probability matrix for 3D iterative reconstruction of MADPET-II data," IEEE Trans. Nucl. Sci. **51**(5), 2597–2605 (2004).
[23]F. R. Rannou and A. F. Chatziioannou, "Fully 3D system model estimation of OPET by Monte Carlo simulation," 2004 IEEE Nuclear Science Symposium Conference Record, Vol. 6, pp. 3433–3436, 2004 (unpublished).
[24]S. Shokouhi *et al.*, "Statistical 3D image reconstruction for the RatCAP PET tomograph using a physically accurate, Monte Carlo based system matrix," 2004 IEEE Nuclear Science Symposium Conference Record, Vol. 6, pp. 3901–3905, 2004 (unpublished).
[25]J. E. Ortuño, P. Guerra-Gutierrez, J. Rubio, G. Kontaxakis, and A. Santos, "3D-OSEM iterative image reconstruction for high-resolution PET using precalculated system matrix," Nucl. Instrum. Methods Phys. Res. A **571**(1–2), 98–101 (2007).
[26]J.-D. Leroux, C. Thibaudeau, R. Lecomte, and R. Fontaine, "Fast, accurate and versatile Monte Carlo method for computing system matrix," IEEE Nuclear Science Symposium Conference Record, 2007 (NSS '07), Vol. 5, pp. 3644–3648, 2007 (unpublished).
[27]L. Zhang, S. Staelens, R. Van Holen, and J. De Beenhouwer, "Fast and memory-efficient Monte Carlo-based image reconstruction for whole-body PET," Med. Phys. **37**(7), 3667–3677 (2010).
[28]N. Rehfeld and M. Alber, "A parallelizable compression scheme for Monte Carlo scatter system matrices in PET image reconstruction," Phys. Med. Biol. **52**, 3421–3437 (2007).
[29]C. Watson, D. Newport, and M. Casey, *A Single-Scatter Simulation Technique for Scatter Correction in 3D PET* (Kluwer Academic, Dordrecht, 1996).
[30]A. Werling, O. Bublitz, J. Doll, L. Adam, and G. Brix, "Fast implementation of the single scatter simulation algorithm and its use in iterative image reconstruction of PET data," Phys. Med. Biol. **47**, 2947–2960 (2002).
[31]J. Ollinger, "Model-based scatter correction for fully 3D PET," Phys. Med. Biol. **41**, 153–176 (1996).
[32]C. Tsoumpas, P. Aguiar, D. Ros, N. Dikaios, and K. Thielemans, "Scatter simulation including double scatter," IEEE Nuclear Science Symposium Conference Record, pp. 3–5, 2005 (unpublished).
[33]A. Rahmim, J. Cheng, S. Blinder, M. Camborde, and V. Sossi, "Statistical dynamic image reconstruction in state-of-the-art high-resolution PET," Phys. Med. Biol. **50**(20), 4887–4912 (2005).
[34]J. Vaquero, E. Lage, L. Rincon, M. Abella, E.Vicente, and M. Desco, "rPET detectors design and data processing," IEEE Nuclear Science Symposium Conference Record, pp. 1–5, 2005 (unpublished).
[35]V. Bettinardi, E. Pagani, M. Gilardi, S. Alenius, K. Thielemans, M. Teras, and F. Fazio, "Implementation and evaluation of a 3d one-step late reconstruction algorithm for 3D positron emission tomography brain studies using median root prior," Eur. J. Nucl. Med. Mol. Imaging **29**(1), 7–18 (2002).
[36]S. Alenius, U. Rutotsalainen, and J. Astola, "Attenuation correction for PET using count-limited transmission images reconstructed with median root prior," IEEE Trans. Nucl. Sci. **46**, 646–651 (1999).
[37]J. E. Ortuño, G. Kontaxakis, J. L. Rubio, P. Guerra, and A. Santos, "Efficient methodologies for system matrix modelling in iterative image reconstruction for rotating high-resolution PET," Phys. Med. Biol. **55**(7), 1833–1861 (2010).
[38]http://physics.nist.gov/PhysRefData/Xcom/Text/XCOM.html.
[39]X. Hua, "Monte Carlo simulation of Comptonization in inhomogeneous media," Comput. Phys. **11**(6), 660–668 (1997).
[40]C. Levin and E. Hoffman, "Calculation of positron range and its effect on the fundamental limit of positron emission tomography system spatial resolution," Phys. Med. Biol. **44**, 781–799 (1999).
[41]depts.washington.edu/simset.
[42]D. Haynor, R. Harrison, and T. Lewellen, "The use of importance sampling techniques to improve the efficiency of photon tracking in emission tomography simulations," Med. Phys. **18**(5), 990–1001 (1991).
[43]A. M. Alessio, C. W. Stearns, S. Tong, S. G. Ross, S. Kohlmyer, A. Ganin, and P. E. Kinahan, "Application and evaluation of a measured spatially variant system model for PET image reconstruction," IEEE Trans. Med. Imaging **29**(3), 938–949 (2010).
[44]S. C. Cherry, J. A. Sorenson, and M. E. Phelps, *Physics in Nuclear Medicine* (Saunders, Philadelphia, 2003).